Dalton Transactions

ROYAL SOCIETY OF CHEMISTRY

FRONTIER

View Article Online
View Journal | View Issue



Cite this: *Dalton Trans.*, 2026, **55**, 3233

# Frontiers in circularly polarized photoluminescence and electroluminescence of chiral manganese(II) complexes

Yong-Hui Zhou [a] and You-Xuan Zheng *[b]

Chiral luminescence materials and their application in biological sensors, mechanoluminescence, triboluminescence, radioluminescence, X-ray scintillation, and circularly polarized organic light-emitting diodes have attracted widespread attention due to their circularly polarized luminescence properties. Among the chiral luminescence materials, phosphorescent complexes with noble metals have been widely investigated, benefiting from their ability to harvest both singlet and triplet excitons in devices. However, although phosphorescent manganese(II) complexes are highly cost-effective and exhibit good luminescence properties and low toxicity, the development of chiral Mn(II) complexes has been slow. This review mainly focuses on the molecular design strategies, photophysical and chiroptical properties, and applications of chiral Mn(II) complexes in different fields while discussing recent progress, challenges and outlook in this area.

Received 10th December 2025,
Accepted 9th January 2026

DOI: 10.1039/d5dt02950c

rsc.li/dalton



## Introduction

Due to their ability to generate circularly polarized luminescence (CPL), chiral materials have potential applications in biological sensors, optical information storage, mechanoluminescence, triboluminescence, radioluminescence, X-ray scintillation, circularly polarized (organic) light-emitting diodes (CP-(O)LEDs), *etc.*[1–7] Among them, CP-(O)LEDs play an important role in 3D display technology. To evaluate the CPL performance of chiral materials and CP-devices, there are two important parameters: dissymmetry factor ($g_{lum}$ ($g_{PL}$ and $g_{EL}$)) and photoluminescence quantum yield (PLQY). Ideal chiral materials should have both high $g_{PL}$ and PLQY values.

Experimentally, the $g_{lum}$ factor is defined as $2 \times \Delta I/I = 2 \times (I_L - I_R)/(I_L + I_R)$, where $I_L$ and $I_R$ represent the intensities of left- and right-handed CPL, respectively. Theoretically, the $g_{lum}$ is defined as $4 \times |\mu_e| \times |\mu_m| \times \cos\theta_{e,m}/(|\mu_e|^2 + |\mu_m|^2)$, where $\mu_e$ and $\mu_m$ denote the electric and magnetic transition dipole moments, respectively, and $\theta_{e,m}$ is the angle between $\vec{\mu}$ and $\vec{m}$. Therefore, chiral materials with similar $\mu_e$ and $\mu_m$ values and $\theta_{e,m}$ near 0° or 180° should show high $g_{PL}$ factors. Furthermore, there is a trade-off relationship between the $\mu_e$ and $\mu_m$, and efficient chiral materials often exhibit large $\mu_e$ values but low $\mu_m$ values. Therefore, most chiral materials show low $g_{lum}$ factors in theory, except for the magnetic transition permitted chiral lanthanide complexes.[8,9]

It is well known that in OLEDs, singlet ($S_1$) and triplet ($T_1$) excitons of the emitters are formed in a 1 : 3 ratio. Over the past decade, significant advancements have been made in chiral fluorescence, thermally activated delayed fluorescence (TADF), and phosphorescence materials.[10–19] For chiral fluorescent materials, only the exciton in the $S_1$ state can be emitted, and 75% of the electrically generated energy in the $T_1$ state is dissipated, leading to a theoretical maximum internal quantum efficiency (IQE) of only 25%. Though TADF materials also emit fluorescence, they can achieve 100% IQE theoretically due to the fast upconversion from $T_1$ to $S_1$ through reverse intersystem crossing. Furthermore, CP-OLEDs with chiral phosphorescent complexes, especially iridium(III) and platinum(II) complexes, can achieve 100% IQE *via* efficient spin–orbit coupling (SOC) effects induced by heavy metal atoms. However, the scarcity and high production cost of these precious-metal-containing materials pose significant challenges. Therefore, chiral phosphorescent complexes based on relatively abundant metals, such as manganese(II) complexes,[20–23] have garnered considerable interest; nevertheless, the development of chiral Mn(II) complexes has been slow.

This frontier article provides a systematic overview of recent advancements in chiral Mn(II) complexes, including their molecular design strategies, photophysical and chiroptical properties, as well as their applications in different areas.

[a]*Jiangsu Key Laboratory of New Energy Devices & Interface Science, School of Chemistry and Materials Science, Nanjing University of Information Science & Technology, Nanjing 210044, P. R. China*
[b]*State Key Laboratory of Coordination Chemistry, School of Chemistry and Chemical Engineering, Nanjing University, Nanjing 210023, P. R. China.*
*E-mail: yxzheng@nju.edu.cn*

# Recent progress in chiral Mn(II) complexes

## Photophysical mechanism for Mn(II) complexes

The Mn(II) ion has 5 single electrons, belonging to the $3d^5$ electron structure, resulting in 16 degenerate spin orbitals according to Hund's rules. For the Mn(II) ion in the tetrahedral ligand field, the singlet orbital $6A_1$ is the ground state and the upper quadruple states $^4E$, $^4A_1$ (G), and $^4E$ (D) have the same slope as the ground state $^6A_1$ on the Tanabe Sugano energy level diagram,[24–26] which explains the electronic transition from the ground state to the high-energy state. Therefore, as shown in Fig. 1(a), the absorption and emission transitions of Mn(II) mainly include the D and G terms. However, the photophysical properties of Mn(II) ions are constrained by their unique excitation mechanism: the d–d transitions of the central metal (Laporte-forbidden) result in an extremely low molar extinction coefficient.[26,27] To overcome this limitation, researchers widely adopted triplet sensitization strategies, enabling efficient energy transfer from organic ligands with suitable energy levels (Fig. 1(b)). The organic ligand acts as the "antenna" to absorb the energy and be excited to the $S_1$ state. Through intersystem crossing, the exciton is transferred to the $T_1$ state of the ligand. Then, the energy is transferred to the excited states of the Mn(II) ion, and the emission corresponding to the characteristic $^4T_1(G) \rightarrow {}^6A_1$ radiative transition is observed. This process must satisfy the following key conditions:[26–29] (1) **Energy level alignment requirement**. The triplet energy level ($E_{T1}$) of the ligand must be higher than the $^4A_1/^4A(G)$ excited state level of Mn(II) (23 256 $cm^{-1} \approx 2.88$ eV). The suitable energy level differences between $E_{T1}$ and $E(^4A_1/^4A(G))$ are within 0.2–0.5 eV, which ensures sufficient driving force for energy transfer while preventing excessive energy gaps that would lead to non-radiative decay. (2) **Spatial coupling effect**. The distance between the ligand and Mn(II) must satisfy the requirements of the Dexter energy transfer mechanism ($r < 10$ Å). (3) **Orbital coupling strength**. The degree of orbital overlap between the ligand and Mn(II) center (characterized by the Hoffmann parameter $\kappa$) must reach above $10^{-3}$, which can be achieved through conjugated ligand design to ensure effective electronic coupling.

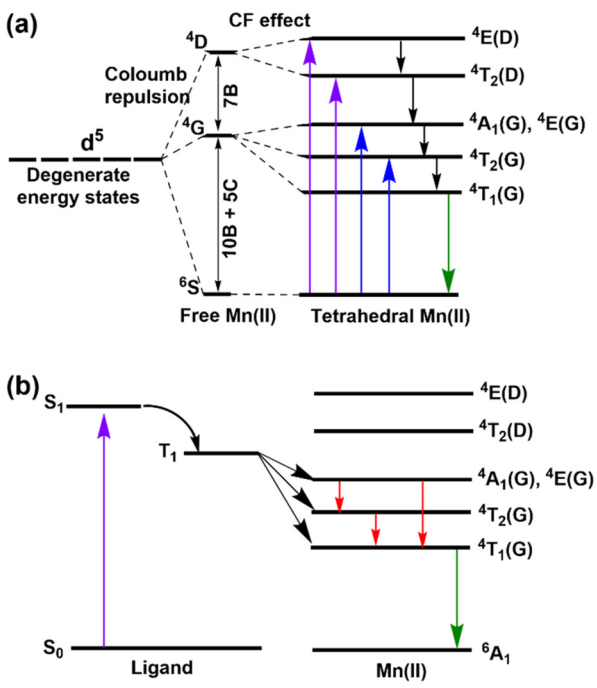


Fig. 1 Luminescence mechanism of a tetrahedral Mn(II) ion (a) and a complex (b).

The organic ligands in Mn(II) complexes primarily consist of electron-donating atoms such as nitrogen or phosphine oxides. The characteristic luminescence of Mn(II) complexes originates from the $^4T_1 \rightarrow {}^6A_1$ radiative transition, a process that is closely related to the crystal field strength ($10D_q$ value).[23] According to crystal field theory, the luminescence of Mn(II) complexes can be systematically regulated through coordination number, ligand field strength, and spatial arrangement, enabling emission from green to near-infrared.

In tetrahedral coordination systems, the Mn(II) ion is typically surrounded by four atoms, forming isolated Mn(II)–ligand units. Under this coordination mode, the crystal field strength is relatively weak ($10D_q \approx 8000$ $cm^{-1}$), and the Mn–Mn distance is large (>5 Å), effectively suppressing spin–spin coupling and resulting in emission wavelengths of 500–550 nm. In contrast, in octahedral coordination systems, forming linear chains within the crystal, the Mn(II) ion is surrounded by six atoms, and the distance between adjacent Mn(II) ions is significantly reduced (≈3.8 Å). This anisotropic structure produces a confinement effect, and, in combination with the stronger crystal field strength ($10D_q \approx 12\,000$ $cm^{-1}$), causes a redshift in the emission wavelength to 580–700 nm. Furthermore, the Mn(II) ion also has three-, five-, seven-, and eight-coordination modes, which provide possibilities for the fine-tuning of the luminescence properties of Mn(II) complexes. Furthermore, most Mn(II) complexes have long phosphorescence lifetimes of up to about 10 ms.

Over the past decade, Mn(II) complexes with diverse coordination types and luminescent colors, along with their applications in triboluminescence, mechanoluminescence, radioluminescence, thermal imaging, temperature sensors, X-ray radioluminescence and scintillation, information recording and security protection, LED and OLED, *etc.*, have drawn significant attention. However, only a few chiral Mn(II) examples have been reported and applied in CP-OLEDs with obvious CP electroluminescence (CPEL).

## Circularly polarized photoluminescence of chiral Mn(II) complexes

In 2020, D. Fu *et al.* reported a pair of perovskite enantiomorphic ferroelectrics, *R*/*S*-3-(fluoropyrrolidinium)$MnBr_3$ (*R*/*S*-1, Fig. 2(a)).[30] The red photoluminescence, peaking at about 650 nm, is produced by octahedrally coordinated Mn(II) ions. *R*/*S*-$MnBr_3$ show mirror-image CPL spectra compatible with

 

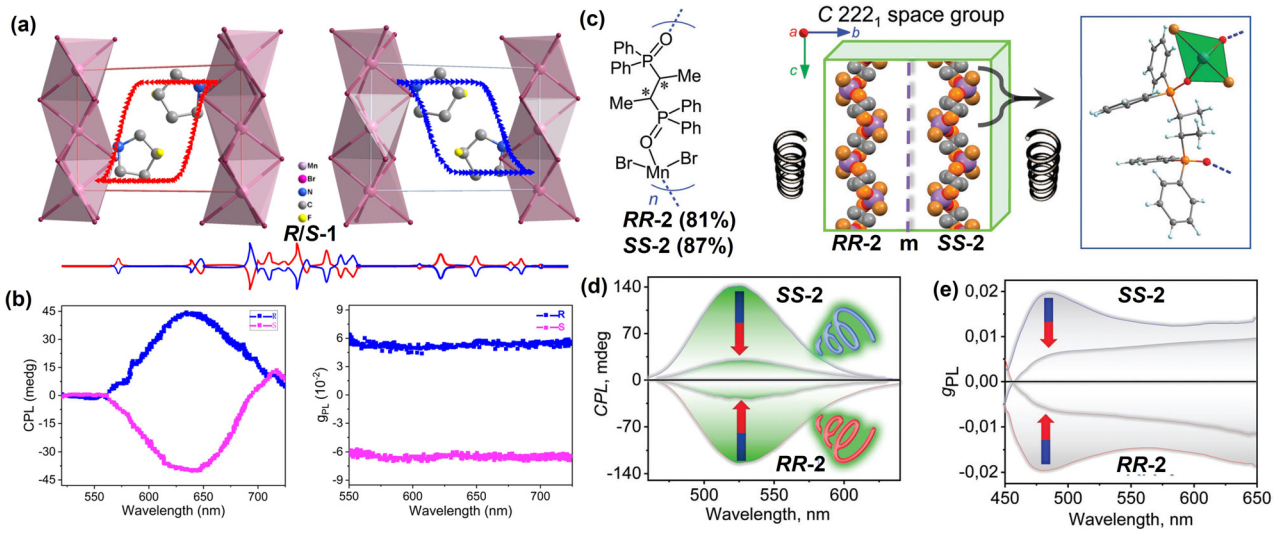


**Fig. 2** (a) Packing views, (b) CPL spectra and $g_{PL}$ – wavelength curves of *R*/*S*-1. Reproduced from ref. 30 with permission from the American Chemical Society, copyright 2020. (c) Ligand and mirrored 1D helical chains of *RR*/*SS*-2 in the crystals (X-ray data). Right: X-ray structure of the repeating unit (the cyan, brown, orange, red, and gray spheres stand for Mn, Br, P, O, and C, respectively); (d) CPL and MCPL spectra and (e) $g_{PL}$ – wavelength curves of *SS*-/*RR*-2: intensity attenuation upon application of a permanent magnetic field (1.6 T). Reproduced from ref. 31 with permission from Wiley-VCH, copyright 2023.

the photoluminescence spectra associated with octahedral Mn(II) ions (Fig. 2(b)). The $g_{PL}$ factors of the enantiomers are ±6.1 × $10^{-3}$ from 550 to 725 nm. The emergence of CPL activity for the two enantiomers, dominated by the space configuration of the octahedral Mn(II) ions, may be attributed to the influence of the introduction of chiral cations. This is the first molecular ferroelectric with CPL activity, holding great potential for the development of new optoelectronic devices.

In 2023, A. V. Artem'ev *et al.* constructed a pair of chiral Mn(II) one-dimensional helical coordination polymers (*RR*/*SS*-2, Fig. 2(c)).[31] The enantiomers emit green emission, peaking at 527 nm, with a PLQY of 89% and an exceptionally high $g_{PL}$ of 2.1 × $10^{-2}$, while remaining ultrarobust toward humidity, temperature, and X-rays. Furthermore, this work revealed for the first time that an external magnetic field exerts a significant negative effect on the CPL of this Mn(II) material. Specifically, under a magnetic field of 1.6 T, the CPL signal was suppressed by a factor of 4.2 times (Fig. 2(d) and (e)). In addition to these properties, the material demonstrates an excellent linear response of emission intensity to temperature over the range of 77–298 K, along with bright mechanoluminescence and outstanding X-ray scintillation activity. Furthermore, the authors also fabricated the UV-pumped CP-LEDs with *RR*/*SS*-2 as phosphors with a large single crystal. The CP-LEDs exhibit strong green emission with only a single band peaking at 528 nm. Interestingly, an optical selectivity of output from the UV-pumped CP-LEDs is demonstrated. By passing through the configured polarizers, the generated light from the chiral emitters produces slightly different intensities. This interesting phenomenon can be explained by the generation of elliptically polarized light after the left circular polarized (LCP) and right circular polarized (RCP) light emitted from *SS*-2 and *RR*-2. More LCP light can pass through the left polarizer, and more RCP light goes through the right polarizer, and a slightly higher intensity of light appears for the corresponding chiral emitters when the direction of the linear polarizer is consistent with the long axis of the elliptically polarized light. This phenomenon also appeared in their other work, in which luminogenic $[MnBr_4]^{2-}$ anions were combined with *R*/*S*-$[MBA\text{-}Me_3]^+$ cations in a single ionic structure (MBA = *R*/*S*-α-methylbenzylamine). The obtained *R*/*S*-$[MBA\text{-}Me_3]MnBr_4$ (*R*/*S*-3) hybrids showed a near-unity PLQY and a high $g_{lum}$ value of 4.5 × $10^{-3}$, and the corresponding UV-pumped CP-LEDs also show excellent optical selectivity.[32]

In 2024, Z. Quan *et al.* reported a pair of zero-dimensional (0D) Mn(II) bromide enantiomers, $[H_2(2R,4R)\text{-}(+)/(2S,4S)\text{-}(-)\text{-}2,4\text{-bis(diphenylphosphino)pentane}]MnBr_4$ (*R*/*S*-4, Fig. 3(a)).[33] By introducing the chiral bisphosphine ligands with rigid bulkiness and rich hydrogen bonds, they achieved the induction of non-centrosymmetric crystal structures. The resulting material exhibits near-unity PLQY and remarkable CPL performance, with $g_{PL}$ values reaching ±2.0 × $10^{-3}$. More importantly, for the first time, this material demonstrates bright circularly polarized mechanoluminescence (CPML) under mechanical stimulation (Fig. 3(b)). It also shows an extremely high sensitivity to weak force stimuli (as low as 0.1 N), significantly outperforming traditional doped inorganic ML materials. Through structure–property relationship analysis, it was found that the excellent CPML performances of *R*/*S*-4 originate from their non-centrosymmetric $P2_1$ space group structure, abundant hydrogen-bonding network, and highly isolated luminescent centers. These features effectively promote the synergistic interaction between cleavage-induced charge separation and luminescent center excitation within

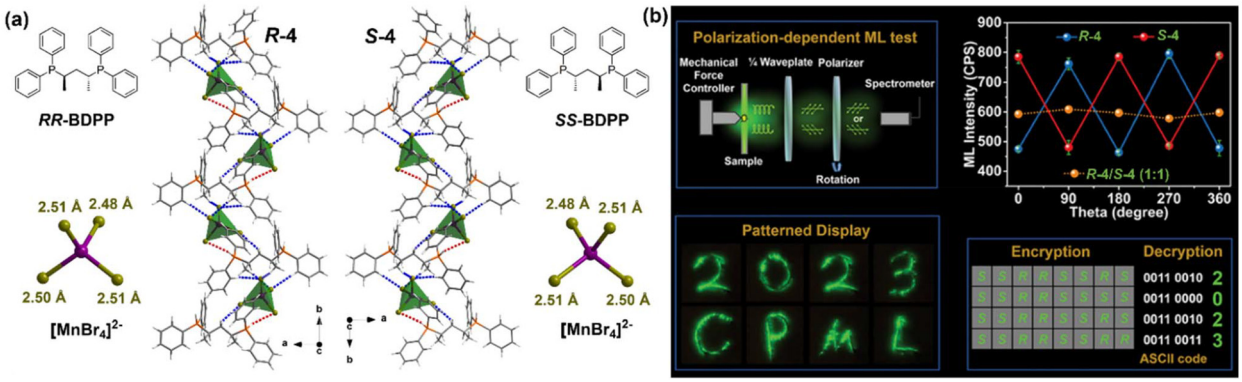


**Fig. 3** (a) *RR*/*SS*-BDPP ligands and $[MnBr_4]^{2-}$ anion structures, and enantiomorphic crystal structures along the *b*-axis in *R*/*S*-4 (Br, Mn, P, C, and H atoms are colored in dark yellow, violet, orange, gray, and white, respectively, and $MnBr_4$ units are displayed as green tetrahedra); (b) schematic of the experimental setup used to characterize CPML in *R*/*S*-4 and polarization-dependent ML emission intensities of chiral *R*-4, *S*-4, and a 1 : 1 racemic mixture of *R*/*S*-4 under 30 N force stimulation. Patterned display of ML emissions in *R*-4. Reproduced from ref. 33 with permission from Wiley-VCH, copyright 2024.

the triboluminescence mechanism. Furthermore, this material exhibits a rare anti-thermal quenching effect across a broad temperature range (300–380 K), which is attributed to a thermally stimulated compensation process between trap states and the $^4T_1$ excited state of Mn(II). Based on their intriguing optical properties, these compounds are demonstrated as chiral force-responsive materials in multilevel confidential information encryption. This work provides a novel strategy and a theoretical foundation for the study of chiral hybrid metal halides in the fields of photonics, information security, flexible electronic devices, and mechano-responsive optical functional materials.

Q. Zhao *et al.* reported a pair of axially chiral Mn(II) enantiomers, *R*/*S*-5 (ligand = 5,5′-bis(diphenylphosphine oxide)-4,4′-bi-1,3-benzodioxole), exhibiting five-coordinated structures.[34] Each Mn(II) ion is coordinated by four O atoms and one Br atom, forming a trigonal bipyramidal geometry (Fig. 4(a)). *R*/*S*-5 exhibit red emission centered at 636 nm, with a PLQY of around 70%. Simultaneously, *R*/*S*-5 demonstrate outstanding CPL properties, featuring $|g_{PL}|$ factors of up to $1.94 \times 10^{-2}$ (Fig. 4(b)). By integrating *S*-5 with commercial phosphors, a white LED was fabricated with good performance. Furthermore, an exceptional scintillation performance was observed, showcasing X-ray imaging with a spatial resolution of up to 11.9 lp $mm^{-1}$.

In 2025, Z. Chen *et al.* reported a pair of Mn(II) hybrid enantiomers, (1*R*/*S*,2*R*/*S*)-(*N*,*N*,*N*′,*N*′-tetramethyl-1,2-cyclohexanediamine)$_2MnBr_4{\cdot}2Br^-$ (*R*/*S*-6), which exhibit high PLQYs of around 94% and intense CPL spectra, with $|g_{PL}|$ factors of around $3.9 \times 10^{-3}$.[35] Furthermore, the enantiomers demonstrate strong scintillation performance with record-breaking light yields of 70 061 and 68 514 photons per MeV in chiral scintillators. This work pioneered the quantitative evaluation of the circularly polarized radioluminescence (CPRL) of *R*/*S*-1, achieving $g_{RL}$ factors of $-2.04 \times 10^{-3}$ and $+2.55 \times 10^{-3}$. By incorporating hydrogen bonds into the structures to facilitate chiral transfer, Mn(II) hybrid enantiomers (1*R*/*S*,2*R*/*S*)-(*N*,*N*′-dimethyl-1,2-cyclohexane-diamine)$MnBr_4$ (*R*/*S*-7, Fig. 4(c)) achieved $|g_{PL}|$ values of around $2.5 \times 10^{-2}$ (Fig. 4(d)), and their $|g_{RL}|$ values also increased to $2.96 \times 10^{-2}$ (Fig. 4(e)). These values substantially surpass those of currently reported lead-free chiral scintillators, representing the state-of-the-art in chiroptical performance for this class of materials. This work manifests a new design strategy for advancing chiral scintillators and establishes a standard approach for evaluating CPRL properties.

Recently, X. Ren *et al.* reported a pair of chiral 0D Mn–Br hybrid enantiomers (*P*/*M*-8) through a crystallization-driven self-assembly strategy using entirely achiral molecular building blocks (Fig. 5).[36] In this system, the interaction between the non-centrosymmetric $[MnBr_4]^{2-}$ and the rotationally symmetric $[Pr\text{-}dabco]^{2+}$ (1-propyl-1,4-diazabicyclo-[2.2.2]octan-1-ium) cation, crystallizing in the chiral space group $P2_12_12_1$, achieved the induction and assembly of a chiral crystal structure. The *P*/*M*-8 single crystals exhibit excellent optical and chiroptical performances, with a PLQY of 68.8% and $|g_{PL}|$ values of up to $4.8 \times 10^{-2}$, respectively. Therefore, this combination achieves the record-high figure of merit of $4.2 \times 10^{-2}$. This study offers a robust strategy for the design and development of high-performance chiral luminescence materials utilizing achiral molecular architectures.

## Circularly polarized electroluminescence of chiral Mn(II) complexes

Because most chiral Mn(II) perovskites, ionic compounds and polymers cannot be evaporated under vacuum, the CPEL was first obtained from CP-LED, fabricated by coating the chiral materials on the UV-LED chip. For example, X. Ren *et al.* fabricated UV-LEDs based on *P*/*M*-8 enantiomers, which demonstrate outstanding performances, with a remarkable luminous brightness (74 591 cd $m^{-2}$), and a high $g_{EL}$ value of $3.2 \times 10^{-2}$ (Fig. 5(d)).[36]

 

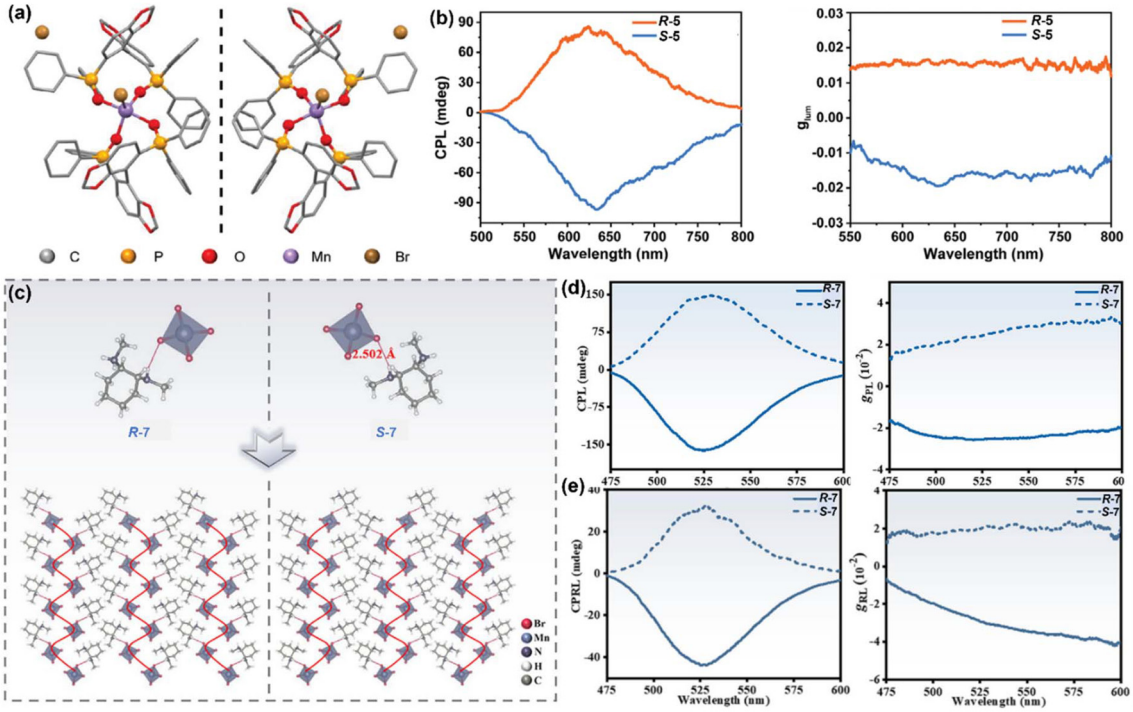


**Fig. 4** (a) Crystal structures, (b) CPL spectra and $g_{PL}$ – wavelength curves of *R*/*S*-5. Reproduced from ref. 34 with permission from Wiley-VCH, copyright 2024. (c) Crystal structures (Br: red, Mn: blue, N: bluish violet, H: white, C: grey); (d) CPL spectra, $g_{PL}$ – wavelength curves and (e) CPRL spectra under X-ray illumination and $g_{RL}$ – wavelength curves of *R*/*S*-7. Reproduced from ref. 35 with permission from Wiley-VCH, copyright 2025.

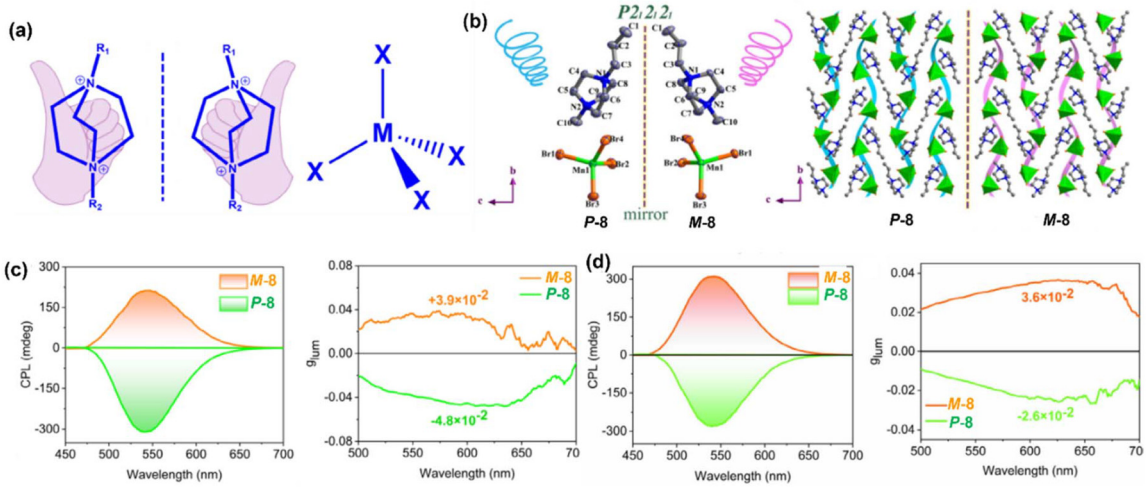


**Fig. 5** (a) Molecular structures of a rotational symmetric $[R_1,R_2\text{-DABCO}]^{2+}$ cation and a tetrahedral $[MnX_4]^{2-}$ anion. (b) Asymmetric unit and enantiomorphic crystal structures of *P*/*M*-8 viewed along the *a*-axis. (c) CPL spectra and $g_{PL}$ – wavelength curves of *P*/*M*-8. (d) CPL spectra of CP-LEDs pumped by 360 nm UV and $g_{EL}$ – wavelength curves of the CP-LEDs at a 5 V driving voltage. Reproduced from ref. 36 with permission from Wiley-VCH, copyright 2025.

In 2024, W.-Y. Wong *et al.* proposed a strategy through steric hindrance-driven bond angle distortion for tuning the color of Mn(II) complexes, based on the dibenzofuran phosphine oxide skeleton.[37] By modulating the steric hindrance between the phosphine and the benzofuran units, as well as altering the O–Mn–O bond angles, five tetrahedral Mn(II) complexes achieve emission wavelengths within 498–548 nm. Interestingly, the single crystals of these achiral Mn(II) complexes exhibit CPL signals due to symmetry breaking. Furthermore, the vacuum-fabricated OLEDs achieve a record

maximum external quantum efficiency ($EQE_{max}$) of 15.7%. Unfortunately, no CPEL signal was observed due to the unstable chiral structure.

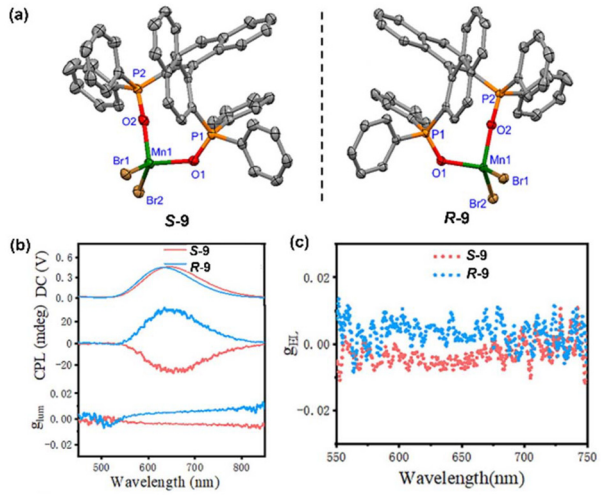


Fig. 6 (a) Single-crystal structures and (b) CPL spectra and $g_{PL}$ – wavelength curves of the *S*/*R*-9 enantiomers. (c) $g_{EL}$ – wavelength curves of the doped devices based on *S*/*R*-9 enantiomers. Reproduced from ref. 38 with permission from the Royal Society of Chemistry, copyright 2025.

In 2024, Z. Chen *et al.* reported a pair of Mn(II) enantiomers (*R*/*S*-9) based on the axially chiral ligands *R*/*S*-2,2′-bis(diphenylphosphinyl)-1,1′-binaphthyl, forming a distorted tetrahedral geometry (Fig. 6(a)).[38] The *R*/*S*-9 enantiomers display orange-red emission with peaks at 633/629 nm with PLQYs of 2.1%/4.0%, respectively. To elucidate the luminescence mechanism, they ruled out the possibilities of Mn–Mn coupling (lattice spacing 8.6 Å) and self-trapped excitons. Calculations using the Tanabe–Sugano diagram yielded a Racah parameter of $B$ = 835.6 $cm^{-1}$ and a crystal field parameter of $D_q$ = 1059.2 $cm^{-1}$, confirming that the strong, high crystal field environment created by the phosphine oxide ligands is the core driving force for the red emission. The enantiomers display $|g_{PL}|$ factors of 5.1 × $10^{-3}$ (Fig. 6(b)). Furthermore, the corresponding solution-processed OLEDs show an $EQE_{max}$ of 4.09% and a $|g_{EL}|$ of 8.5 × $10^{-3}$ (Fig. 6(c)).

Nearly at the same time, our group reported two pairs of chiral Mn(II) enantiomers (*R*/*S*-10 and *R*/*S*-11, Fig. 7(a)) based on phosphorus central chiral ligands, *tert*-butyl(6-(diphenylphosphoryl)dibenzo[*b*,*d*]furan-4-yl)(phenyl)phosphine oxide and *tert*-butyl(5-(diphenylphosphoryl)-9,9-dimethyl-9*H*-xanthen-4-yl)(phenyl)phosphine oxide.[39] The *R*/*S*-10 and *R*/*S*-11 enantiomers exhibit yellow-green emission, peaking at 541 and 532 nm (Fig. 7(b)), with PLQYs of 87% and 77% in the solid state, respectively. Structural variations in the ligand backbones significantly impacted their emission properties.

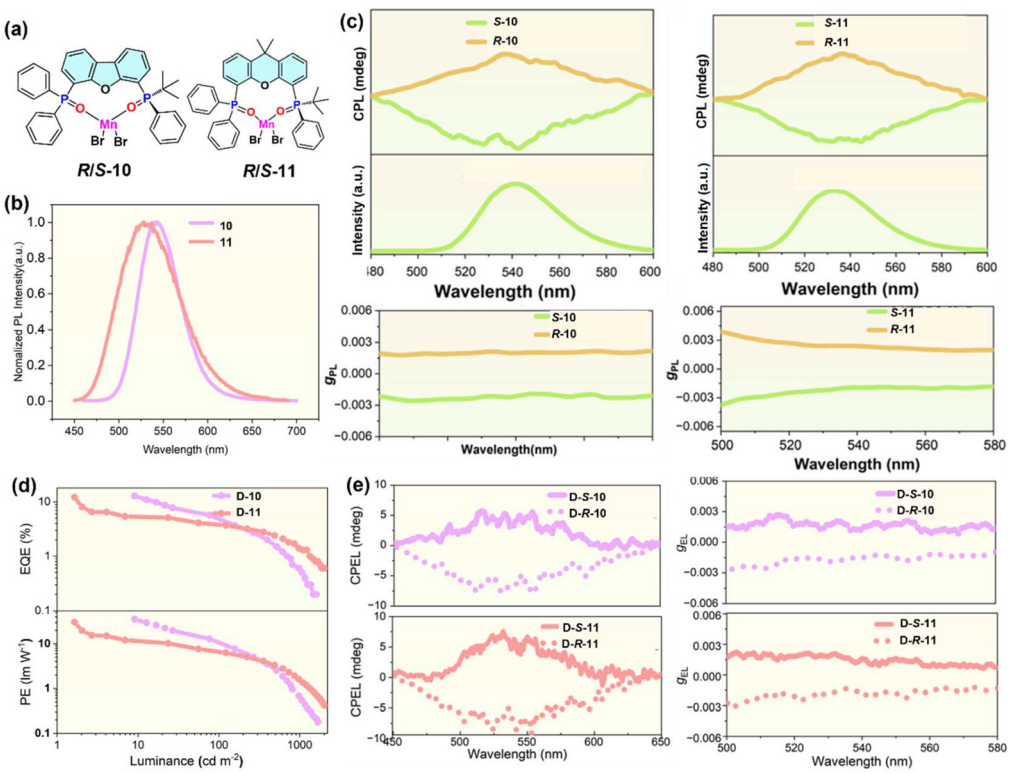


Fig. 7 (a) Molecular structures, (b) PL spectra, (c) CPL spectra and $g_{PL}$ – wavelength curves of the *R*/*S*-10 and *R*/*S*-11 enantiomers. (d) External quantum efficiency–luminance curves of D-10 and D-11 (OLEDs based on *rac*-10 and *rac*-11). (e) CPEL spectra and $g_{EL}$ – wavelength curves of D-*R*/*S*-10 and D-*R*/*S*-11 (CP-OLEDs based on *R*/*S*-10 and *R*/*S*-11 enantiomers). Reproduced from ref. 39 with permission from Wiley-VCH, copyright 2025.

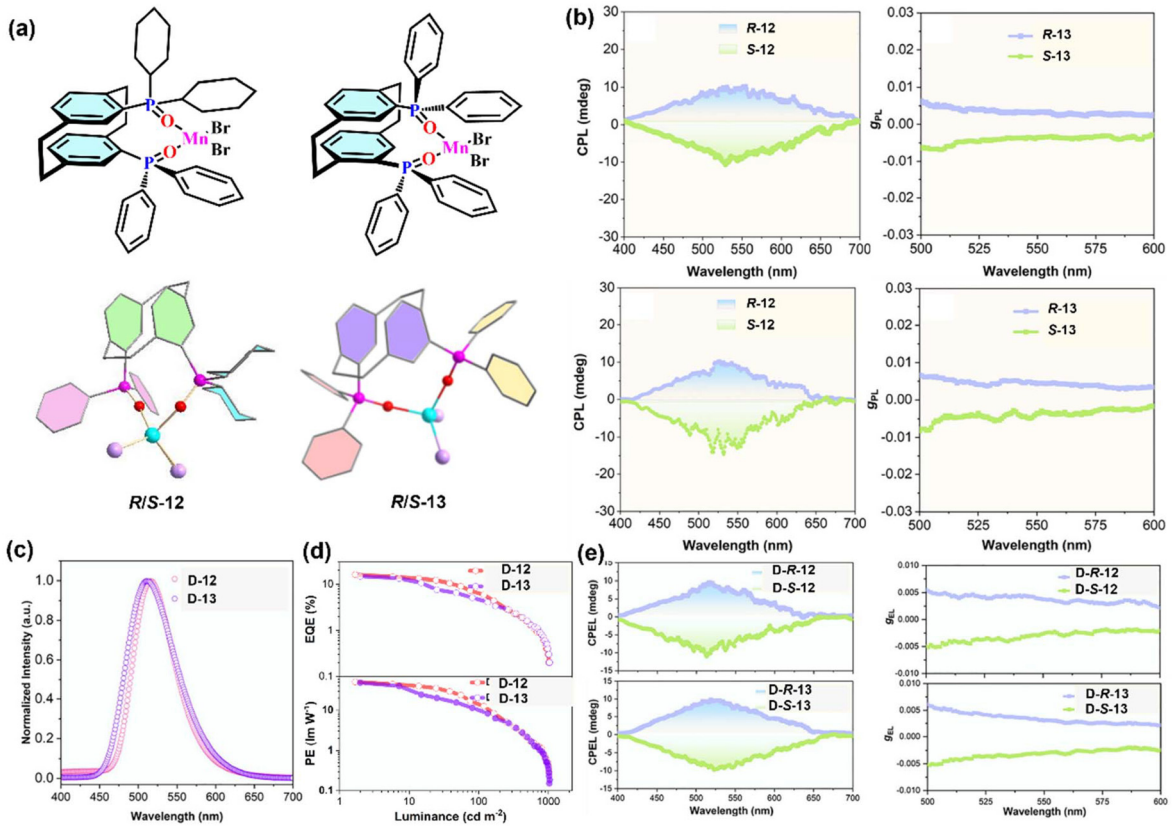


**Fig. 8** (a) Molecular and single-crystal structures, (b) CPL spectra and $g_{PL}$ – wavelength curves of the *R*/*S*-12 and *R*/*S*-13 enantiomers. (c) EL spectra and (d) EQE–PE-luminance curves of OLEDs based on racemic 12 and 13 complexes. (e) CPEL spectra and $g_{EL}$ – wavelength curves of the CP-OLEDs based on *R*/*S*-12 and *R*/*S*-13 enantiomers. Reproduced from ref. 40 with permission from Science China Press and Springer, copyright 2025.

The rigid five-membered ring in DFPO led to denser packing and a higher radiative decay rate (2018 $s^{-1}$), compared to the more flexible six-membered XTDPO (1037 $s^{-1}$), thus resulting in a higher PLQY for complex 10. The $|g_{PL}|$ values of *R*/*S*-10 and *R*/*S*-11 enantiomers are $2.0 \times 10^{-3}$ and $2.2 \times 10^{-3}$ (Fig. 7(c)), respectively. The corresponding vacuum-fabricated CP-OLEDs based on *R*/*S*-10 and *R*/*S*-11 deliver $EQE_{max}$ values of 12.9% and 12.2% (Fig. 7(d)), with $|g_{EL}|$ factors of $1.5 \times 10^{-3}$ and $1.8 \times 10^{-3}$ (Fig. 7(e)), respectively. These findings validate the use of phosphorus-centered chiral ligands in constructing chiral Mn(II) complexes for efficient CP-OLEDs.

Recently, to further enhance both the $g_{lum}$ value and the device efficiency of the chiral Mn(II) complexes, [2.2]paracyclophane (pCp) was employed as a rigid planar chiral scaffold.[40] Chiral ligands were obtained by introducing phosphine oxide groups at the 4,13- and 4,12-positions of pCp, which were subsequently coordinated with $MnBr_2$ to afford two pairs of enantiomers: *R*/*S*-12 and *R*/*S*-13 (Fig. 8(a)). The rigid aromatic backbone and extended Mn–Mn distances of the Mn(II) complexes suppressed non-radiative losses, resulting in green emission with high PLQYs of up to 90%. Furthermore, the $|g_{PL}|$ values of *R*/*S*-12 and *R*/*S*-13 enantiomers reach $4.2 \times 10^{-3}$ and $4.0 \times 10^{-3}$ (Fig. 8(b)), respectively, which can be attributed to efficient chiral electronic transitions across the pCp framework. OLEDs based on the racemic complexes display notable $EQE_{max}$ values of up to 16.0% (Fig. 8(d)), the highest for Mn(II) complex-based OLEDs to date. In addition, the CP-OLEDs incorporating *R*/*S*-12 and *R*/*S*-13 enantiomers show high $|g_{EL}|$ values of $4.5 \times 10^{-3}$ and $4.3 \times 10^{-3}$ (Fig. 8(e)), approximately 2.5 times greater than those of their phosphorus central chiral analogues. This work reports the first planar chiral Mn(II) complexes and offers a valuable design strategy for the development of high-performance chiral emitters for CP-OLEDs.

## Conclusion and outlook

In conclusion, significant advancements of chiral Mn(II) complexes have been achieved in recent years, demonstrating their potential in multifunctional optoelectronic devices. However, there are only a few isolated examples of chiral organic complexes, chiral polymers, 0D Mn–Br hybrid enantiomers and perovskites that have been applied in circularly polarized mechanoluminescence and triboluminescence, X-ray scintillation and imaging activity, radioluminescence and LED/OLED, *etc*. To date, only three examples of chiral Mn(II) complexes have been reported for CP-OLEDs in the literatures. The design of novel chiral Mn(II) complexes that possess high

luminescence efficiency and excellent chiroptical properties (high $g_{lum}$ values, especially), remains a significant challenge. In our opinion, attention should be paid to the following aspects of research:

**Molecular design and optical tuning mechanisms need to be clarified**

Although different types of chiral Mn(II) frameworks have been investigated, systematic theoretical guidance is still lacking. Especially, the maximum $g_{lum}$ factors of chiral Mn(II) enantiomers are still at the $10^{-2}$ level. Specifically, how to achieve predictable control over emission wavelength, emission bandwidth, excited-state dynamics, and CPL property of chiral Mn(II) enantiomers through precise manipulation of ligand electronic structure, steric hindrance, and chiral environment requires further exploration. Current tuning methods still heavily rely on empirical accumulation and trial-and-error approaches, lacking universal design rules. This limits the expansion of chiral Mn(II) materials towards broader emission ranges and better CPL properties with high $g_{PL}$ factors. Future efforts should integrate theoretical calculations to establish interpretable structure–property relationship models between ligands and chiroptical behaviours of chiral Mn(II) complexes, enabling more efficient spectral region control and innovative molecular design.

**Luminescence lifetime regulation mechanisms require breakthroughs**

As a first-row transition metal, Mn(II) exhibits weak SOC effects, and its luminescence typically manifests as phosphorescence from its triplet state with a long decay lifetime. Therefore, the chiral Mn(II) complexes exhibit emission lifetimes on the order of hundreds of microseconds, reflecting the spin-forbidden nature of the emission process to some extent. But the long lifetimes of the chiral Mn(II) complexes also introduce a series of issues. In particular, it can easily induce exciton annihilation in OLEDs, such as triplet–triplet annihilation and triplet-polaron annihilation, leading to a severe efficiency roll-off in the devices at high brightness. Therefore, it is necessary to design suitable ligands to regulate chiral organic–inorganic hybrid and organic Mn(II) frameworks with short excited-state lifetimes.

**CPEL device engineering still faces challenges**

Although some chiral Mn(II) complexes have been applied in CP-OLEDs, their performances in key parameters such as brightness, efficiency, efficiency roll-off, and device stability still lag behind those of chiral TADF materials and Ir(III) complexes. Concurrently, most current devices employ non-doped structures or simple doping strategies, lacking in-depth control and systematic optimization of device physics mechanisms such as charge injection, transport, and recombination interfaces. In particular, most chiral Mn(II) hybrid materials cannot be evaporated and have poor solubility in most organic solvents. Follow-up research should strengthen the synergistic regulation of device structures by developing better-matched functional layers, solution-processing methods, and even using crystal as the emissive layer directly.

**Multiple types of applications need to be expanded**

As discussed above, circularly polarized X-ray scintillation and imaging, radioluminescence, mechanoluminescence and triboluminescence, and CP-LEDs/CP-OLEDs have been explored based on chiral Mn(II) complexes. However, further exploration is needed for chiral Mn(II) complexes in other fields. Meanwhile, current research is still limited at the laboratory level, and there is still a significant gap to practical applications. Furthermore, due to stability factors, current research mainly focuses on divalent chiral Mn(II) materials, with emission wavelengths from green to near-infrared. The research in chiral Mn complexes with other valence, such as Mn(IV) hybridization or inorganic structures, has never been reported. We think it is an interesting research direction in the future, providing the possibility in obtaining chiral Mn complexes and devices in a larger spectral range.

## Conflicts of interest

There are no conflicts to declare.

## Data availability

No primary research results, software or code have been included and no new data were generated or analysed as part of this frontier article.

## Acknowledgements

This work was supported by the National Natural Science Foundation of China (U23A20593).

## References

1 J. R. Brandt, F. Salerno and M. J. Fuchter, *Nat. Rev. Chem.*, 2017, **1**, 0045.
2 Y. Sang, J. Han, T. Zhao, P. Duan and M. Liu, *Adv. Mater.*, 2020, **32**, 1900110.
3 L. Frédéric, A. Desmarchelier, L. Favereau and G. Pieters, *Adv. Funct. Mater.*, 2021, **31**, 2010281.
4 D.-W. Zhang, M. Li and C.-F. Chen, *Chem. Soc. Rev.*, 2020, **49**, 1331–1343.
5 Z.-L. Gong, X. Zhu, Z. Zhou, S.-W. Zhang, D. Yang, B. Zhao, Y.-P. Zhang, J. Deng, Y. Cheng, Y.-X. Zheng, S.-Q. Zang, H. Kuang, P. Duan, M. Yuan, C.-F. Chen, Y. S. Zhao, Y.-W. Zhong, B. Z. Tang and M. Liu, *Sci. China Chem.*, 2021, **64**, 2060–2104.
6 X. Yang, X. Gao, Y.-X. Zheng, H. Kuang, C.-F. Chen, M. Liu, P. Duan and Z. Tang, *CCS Chem.*, 2023, **5**, 2760–2789.

 

7 L. Yuan, Y.-P. Zhang and Y.-X. Zheng, *Sci. China Chem.*, 2024, **67**, 1097–1116.
8 F. Zinna, U. Giovanella and L. Di Bari, *Adv. Mater.*, 2015, **27**, 1791–1795.
9 F. Zinna, L. Arrico, T. Funaioli, L. Di Bari, M. Pasini, C. Bottab and U. Giovanella, *J. Mater. Chem. C*, 2022, **10**, 463–468.
10 X.-F. Luo, H.-B. Han, Z.-P. Yan, Z.-G. Wu, J. Su, J.-W. Zou, Z.-Q. Zhu, Y.-X. Zheng and J.-L. Zuo, *ACS Appl. Mater. Interfaces*, 2020, **12**, 23172–23180.
11 T.-Y. Li, Y.-M. Jing, X. Liu, Y. Zhao, L. Shi, Z. Tang, Y.-X. Zheng and J.-L. Zuo, *Sci. Rep.*, 2015, **5**, 14912.
12 M. Li, S.-H. Li, D. Zhang, M. Cai, L. Duan, M.-K. Fung and C.-F. Chen, *Angew. Chem., Int. Ed.*, 2018, **57**, 2889–2893.
13 Z.-G. Wu, H.-B. Han, Z.-P. Yan, X.-F. Luo, Y. Wang, Y.-X. Zheng, J.-L. Zuo and Y. Pan, *Adv. Mater.*, 2019, **31**, 1900524.
14 M. Li, Y.-F. Wang, D. Zhang, L. Duan and C.-F. Chen, *Angew. Chem., Int. Ed.*, 2020, **59**, 3500–3504.
15 S.-Y. Yang, Y.-K. Wang, C.-C. Peng, Z.-G. Wu, S. Yuan, Y.-J. Yu, H. Li, T.-T. Wang, H.-C. Li, Y.-X. Zheng, Z.-Q. Jiang and L.-S. Liao, *J. Am. Chem. Soc.*, 2020, **142**, 17756–17765.
16 W. Yang, N. Li, J. Miao, L. Zhan, S. Gong, Z. Huang and C. Yang, *CCS Chem.*, 2022, **4**, 3463–3471.
17 Q. Wang, L. Yuan, C. Qu, T. Huang, X. Song, Y. Xu, Y.-X. Zheng and Y. Wang, *Adv. Mater.*, 2023, **35**, 2305125.
18 L. Yuan, Y.-F. Yang, Z.-P. Yan, J.-J. Hu, D. Mao, H.-X. Ni and Y.-X. Zheng, *Adv. Funct. Mater.*, 2024, **34**, 2403803.
19 X.-J. Liao, S. Xing, J.-J. Hu, X.-Z. Wang and Y.-X. Zheng, *CCS Chem.*, 2025, **7**, 2419–2431.
20 L.-J. Xu, C.-Z. Sun, H. Xiao, Y. Wu and Z.-N. Chen, *Adv. Mater.*, 2017, **29**, 1605739.
21 Y. Qin, P. Tao, L. Gao, P. She, S. Liu, X. Li, F. Li, H. Wang, Q. Zhao, Y. Miao and W. Huang, *Adv. Optical Mater.*, 2018, **6**, 1801160.
22 P. Tao, S.-J. Liu and W.-Y. Wong, *Adv. Optical Mater.*, 2020, **8**, 2000985.
23 Y. Qin, P. She, X. Huang, W. Huang and Q. Zhao, *Coord. Chem. Rev.*, 2020, **416**, 213331.
24 C. Albert, G. David and M. Goodgame, *J. Am. Chem. Soc.*, 1962, **84**, 167–172.
25 M. T. Vala, C. J. Ballhausen, R. Dingle and S. L. Holt, *Mol. Phys.*, 1972, **23**, 217.
26 Q. Zhou, L. Dolgov, A. M. Srivastava, L. Zhou, Z. Wang, J. Shi, M. D. Dramic'anin, M. G. Brikefg and M. Wu, *J. Mater. Chem. C*, 2018, **6**, 2652–2671.
27 V. Morad, I. Cherniukh, L. Pöttschacher, Y. Shynkarenko, S. Yakunin and M. V. Kovalenko, *Chem. Mater.*, 2019, **31**, 10161–10169.
28 J. Chen, Q. Zhang, F. Zheng, Z. Liu, S. Wang, A. Wu and G. Guo, *Dalton Trans.*, 2015, **44**, 3289–3294.
29 B. Su, M. S. Molokeev and Z. Xia, *J. Mater. Chem. C*, 2019, **7**, 11220–11226.
30 J.-X. Gao, W.-Y. Zhang, Z.-G. Wu, Y.-X. Zheng and D.-W. Fu, *J. Am. Chem. Soc.*, 2020, **142**, 4756–4761.
31 M. P. Davydova, L. Meng, M. I. Rakhmanova, Z. Jia, A. S. Berezin, I. Y. Bagryanskaya, Q. Lin, H. Meng and A. V. Artem'ev, *Adv. Mater.*, 2023, **35**, 2303611.
32 M. P. Davydova, L. Meng, M. I. Rakhmanova, I. Y. Bagryanskaya, V. S. Sulyaeva, H. Meng and A. V. Artem'ev, *Adv. Optical Mater.*, 2023, **11**, 2202811.
33 X. He, Y. Zheng, Z. Luo, Y. Wei, Y. Liu, C. Xie, C. Li, D. Peng and Z. Quan, *Adv. Mater.*, 2024, **36**, 2309906.
34 Z. Zhou, T. Jiang, Y. Yang, Y. Deng, M. Wang, Y. Ma, S. Liu and Q. Zhao, *Adv. Optical Mater.*, 2024, **12**, 2302185.
35 J.-Y. Yao, Q.-R. Ding, H. Zeng, J.-Y. Wang, C.-M. Shi, L.-J. Xu and Z.-N. Chen, *Angew. Chem., Int. Ed.*, 2025, **64**, e202502099.
36 L. Zhai, J. Yuan, J. Huang, X.-W. Pan, L. Wan, W. Ning and X.-M. Ren, *Angew. Chem., Int. Ed.*, 2025, **64**, e202425543.
37 P. She, Z. Zheng, Y. Qin, F. Li, X. Zheng, D. Zhang, Z. Xie, L. Duan and W.-Y. Wong, *Adv. Optical Mater.*, 2024, **12**, 2302132.
38 D.-H. Kong, Y. Wu, C.-M. Shi, H. Zeng, L.-J. Xu and Z.-N. Chen, *Chem. Sci.*, 2024, **15**, 16698–16704.
39 Z.-Z. Huo, Y. Wang, B. Yang, J.-Q. Liang, X.-F. Hong, Q. An, L. Yuan, H. Ma, J.-L. Zuo and Y.-X. Zheng, *Adv. Optical Mater.*, 2025, **13**, 2402684.
40 Z.-Z. Huo, X.-F. Hong, Y. Wang, X.-S. Zhong, X. Xiao, L. Yuan, Y.-H. Zhou and Y.-X. Zheng, *Sci. China Chem.*, 2025, **68**, 5673–5681.